# A Low-Level Circulation in the Tropics

IAN FOLKINS

*Department of Physics and Atmospheric Science, Dalhousie University, Halifax, Nova Scotia, Canada*

S. FUEGLISTALER

*Institute for Atmosphere and Climate, ETH Zurich, Zurich, Switzerland*

G. LESINS AND T. MITOVSKI

*Department of Physics and Atmospheric Science, Dalhousie University, Halifax, Nova Scotia, Canada*

(Manuscript received 15 March 2007, in final form 23 May 2007)

ABSTRACT

Deep convective tropical systems are strongly convergent in the midtroposphere. Horizontal wind measurements from a variety of rawinsonde arrays in the equatorial Pacific and Caribbean are used to calculate the mean dynamical divergence profiles of large-scale arrays ($\geq$1000 km in diameter) in actively convecting regions. Somewhat surprisingly, the magnitude of the midtropospheric divergence calculated from these arrays is usually small. In principle, the midlevel convergence of deep convective systems could be balanced on larger scales either by a vertical variation in the radiative mass flux of the background clear sky atmosphere, or by a divergence from shallow cumuli. The vertical variation of the clear sky mass flux in the midtroposphere is small, however, so that the offsetting divergence must be supplied by shallow cumuli. On spatial scales of ~1000 km, the midlevel convergent inflow toward deep convection appears to be internally compensated, or "screened," by a divergent outflow from surrounding precipitating shallow convection. Deep convective systems do not induce a large-scale inflow of midlevel air toward actively convecting regions from the rest of the tropics, but instead help generate a secondary low-level circulation, in which the net downward mass flux from mesoscale and convective-scale downdrafts is balanced by a net upward mass flux from precipitating shallow cumuli. The existence of this circulation is consistent with observational evidence showing that deep and shallow convection are spatiotemporally coupled on a wide range of both spatial and temporal scales. One of the mechanisms proposed for coupling shallow convection to deep convection is the tendency for deep convection to cool the lower troposphere. The authors use radiosonde temperature profiles and the Tropical Rainfall Measuring Mission (TRMM) 3B42 gridded rainfall product to argue that the distance over which deep convection cools the lower troposphere is approximately 1000 km.

## 1. Introduction

In the tropics, convective clouds are often considered to fall into one of three categories: boundary layer, shallow, or deep (Johnson et al. 1999). Boundary layer convective clouds contribute to an upward eddy flux of heat and moisture from the surface, are usually nonprecipitating, and rarely penetrate the 2-km local maximum in static stability. Most of the rainfall in the tropics is associated with deep cumulonimbus and stratiform clouds, whose outflow is preferentially distributed between 10 and 17 km, and gives rise to the large-scale Hadley–Walker circulation. A variety of evidence supports the existence of a distinct intermediate cloud type. This intermediate cloud type is usually referred to as shallow convection. It is primarily composed of cumulus congestus clouds, though some fraction of these clouds will later develop into cumulonimbus clouds. Model simulations, and measurements from spaceborne lidars, indicate that the most probable cloud-top altitude for this cloud type is 5–6 km (Redelsperger et al. 2002; Dessler et al. 2006), with some shallow convective clouds rising as high as 8 km (May and Rajo-

*Corresponding author address:* Ian Folkins, Department of Physics and Atmospheric Science, Dalhousie University, Halifax NS B3H 3J5, Canada.
E-mail: ian.folkins@dal.ca

DOI: 10.1175/2007JAS2463.1

padhaya 1996; Trenberth et al. 2000; Jensen and Del Genio 2006). It has been suggested that shallow convective clouds were responsible for about 28% of the convective rainfall over the western Pacific warm pool during the Tropical Ocean and Global Atmosphere Coupled Ocean–Atmosphere Response Experiment (TOGA COARE; Johnson et al. 1999).

It is sometimes argued that shallow convective clouds do not constitute a distinct convective cloud type, but simply reflect an increased propensity for boundary layer clouds to penetrate the boundary layer inversion as one approaches actively convecting regions. Indeed, the abrupt decrease in climatological relative humidity at the top of the boundary layer does diminish in regions of active deep convection, and sometimes disappears entirely. However, the persistence of an abrupt change in static stability near 2 km suggests that mixing processes in the boundary layer continue to be distinct from the overlying troposphere even in regions of active deep and shallow convection. Radar measurements also show the continued existence of a discrete boundary layer mode when cumulus congestus clouds are present (Jensen and Del Genio 2006).

Observational and modeling studies have demonstrated that the best local predictor for the subsequent development of deep convection is increased relative humidity in the mid- and lower troposphere (Sherwood 1999; Tompkins 2001; Grabowski 2003). The enhanced relative humidity that precedes deep convection is usually due to an increase in shallow convection (Mapes et al. 2006; Tulich et al. 2007).

While shallow convection aids the subsequent development of deep convection, deep convection can trigger the development of shallow convection. There are two mechanisms by which this occurs. The first mechanism involves surface cold pools generated by mesoscale downdrafts from precipitating stratiform anvils. These surface cold pools can trigger shallow convection along their leading edge. The second mechanism has been termed "action at a distance" (Fovell 2006). By mass continuity, the net vertical displacements of mass within convective updrafts and downdrafts must be balanced by compensating vertical mass fluxes in the background atmosphere. During the latter stages of the convective life cycle, evaporative cooling from stratiform downdrafts generates gravity waves that induce a net compensatory uplift in their environment (e.g., Mapes and Houze 1995). The negative temperature and positive relative humidity anomalies associated with this uplift increase the buoyancy and growth rates of any preexisting shallow cumuli, and increase the likelihood that a shallow convective cloud will develop into a deep convective cloud. The two-way interaction between deep and shallow convection is believed to play an important role in the propagation of coherent tropical rainfall patterns, such as the Madden–Julian oscillation (Kiladis et al. 2005).

The shallow cumuli triggered by a spreading cold pool occur in the immediate mesoscale vicinity of a precipitating stratiform anvil. The shallow cumuli triggered during the ascending phase of a propagating gravity wave can occur at much farther distances from the anvil cloud. In the first part of this paper we show that the negative temperature anomalies in the lower troposphere associated with increased deep convection (Zipser 1977; Sherwood et al. 2003) have a spatial extent of roughly 1000 km in the equatorial Pacific.

The most outstanding feature of dynamical divergence profiles obtained from actively convecting regions is a layer of pronounced divergence in the upper troposphere (e.g., Yanai et al. 1973; Betts 1973). Radar and rawinsonde measurements have demonstrated that mesoscale deep convective systems are convergent in the midtroposphere (Mapes and Houze 1995; Mapes et al. 2006). In the second part of this paper, we use horizontal wind measurements from tropical rawinsonde stations to calculate the climatological dynamical divergence profiles of several regions. These regions are typically 1000 km or larger in diameter. A field of precipitating shallow cumuli would be expected to give rise to a divergent outflow in the mid- and lower troposphere. The dynamical divergence of an actively convecting region could in principle be convergent or divergent in the midtroposphere, depending on its relative mix of deep and shallow convection. We find, however, that the magnitude of the midtropospheric dynamical divergence in actively convecting large-scale regions is usually near zero. This cancellation appears to be a consequence of the observed spatiotemporal coupling between deep and shallow convection (Kiladis et al. 2005; Mapes et al. 2006).

In actively convecting regions of the tropics, the variation of the lapse rate with altitude in the lower troposphere is inconsistent with both the reversible moist adiabatic or pseudoadiabatic idealizations (Mapes 2001; Folkins 2006). In the third part of this paper, we discuss the relationship between the regional low-level shallow/downdraft circulation and the density structure of the lower troposphere.

## 2. Impact of deep convection on temperature

The left-hand side of Fig. 1 shows the temperature response at Koror (7.3°N) to enhanced rainfall occurring within various distances of Koror. Koror is an island in the western tropical Pacific. Its location is shown

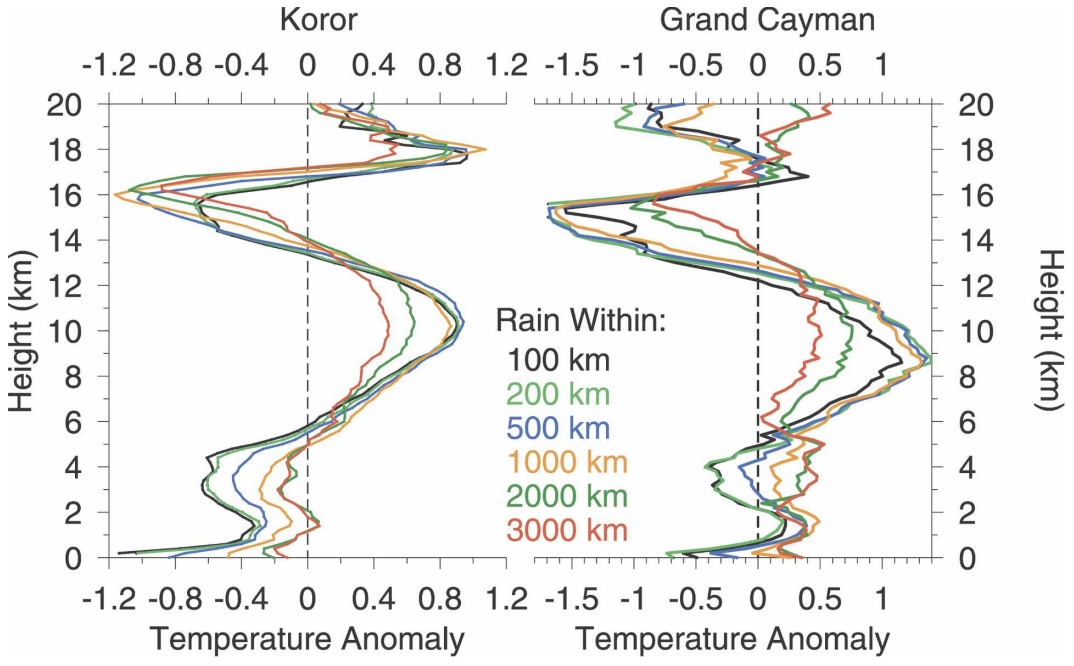


FIG. 1. (left) The temperature anomaly at Koror (7.3°N), averaged over times in which the instantaneous average rainfall rate within circles of various radii centered at Koror is in the top 10% for that month. The temperature anomaly is defined with respect to the monthly mean. (right) The convective temperature anomaly profiles at Grand Cayman (19.3°N).

in Fig. 2. The temperature anomaly has been defined with respect to the local monthly mean. The monthly mean temperature profile was determined from twice daily radiosonde profiles from 1998 to 2004. At each radiosonde measurement time, we used the Tropical Rainfall Measuring Mission (TRMM) 3B42 rainfall product to find the average rainfall rate within circles of various radii centered at Koror. The TRMM 3B42 rainfall dataset has a horizontal resolution of 0.25° and temporal resolution of 3 h. The profiles shown in Fig. 1 represent the mean temperature anomaly during times when the average rainfall within a circle of a given radii is in the top 10 percentile for that month.

In agreement with previous studies, convection is associated with reduced temperatures in the lower troposphere, increased temperatures from 5 to 14 km, and lower temperatures between 14 and 17 km. The structure of the temperature anomaly pattern between 2 and 14 km is suggestive of a superposition of a "convective" mode, reflecting heating from 2 to 14 km, and a "stratiform" mode, consisting of lower-tropospheric cooling and upper-tropospheric heating (Houze 1989). The amplitude of the stratiform mode appears to decay more rapidly with distance from convection than does the convective mode, so that on large spatial scales, rainfall tends to warm the tropical troposphere at most altitudes below 14 km.

The analysis discussed above for Koror was carried out at eight other high-resolution tropical radiosonde stations. The right-hand side of Fig. 1 shows the results for Grand Cayman (19.3°N). Grand Cayman is an island in the Caribbean Sea. Its location is shown in Fig. 3. It is difficult to directly intercompare temperature anomalies from different stations, in part because the rainfall fields around the stations are quite different. However, the overall patterns are similar.

Figure 4 shows the seasonal variation of monthly mean rainfall at each radiosonde station, averaged over a circle with radius of 500 km. Rainfall rates were again obtained from the TRMM 3B42 1999–2005 dataset. The temperature profile is unlikely to be strongly affected by local deep convection during periods in which the monthly mean rainfall rate is very low. The temperature anomalies shown in Fig. 1, and for all other radiosonde stations, were therefore averaged only over months in which the mean rainfall rate exceeded 3.4 mm $day^{-1}$. As a result, the statistical representativeness of the temperature anomaly profiles at the Caribbean stations is weaker than at the Pacific stations. At Seawell, Barbados, and San Juan, Puerto Rico, for example, only two months of data per year were available to construct the temperature anomaly profiles.

While the overall temperature anomaly pattern at Grand Cayman is similar to Koror, the negative tem-

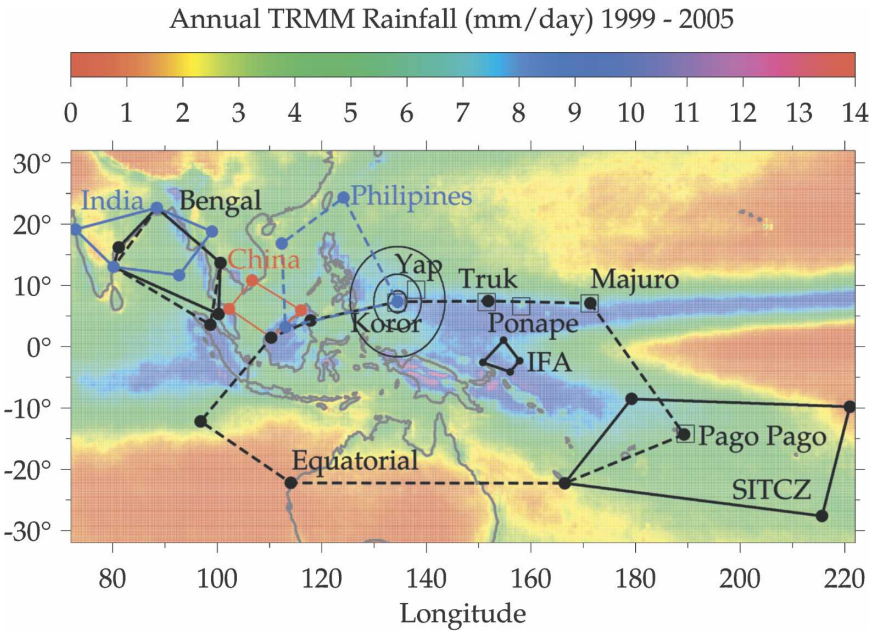


FIG. 2. A map showing the various rawinsonde arrays used to calculate the dynamical divergence profiles, superimposed on annual mean TRMM rainfall (1999–2005). The arrays have been drawn in different colors to help distinguish them from each other—India: blue, Bay of Bengal: solid black and dashed black, South China Sea: red, Philippines: dashed blue, equatorial: dashed black, SITCZ: solid black, and IFA: solid black. Six of the high-resolution U.S. radiosonde stations are denoted by open boxes: Koror, Yap, Truk, Ponape, Majuro, and Pago Pago. The circles centered on Koror have radii equal to 500 and 1000 km.

perature perturbations at Grand Cayman have a shorter spatial range. In Fig. 5, the lower-tropospheric response (averaged from 2.5 to 4.5 km) and the full-depth tropospheric response (averaged from 2.0 to 14.0 km) are plotted against the radius of the circle over which rainfall is being averaged. The solid curves refer to stations in the Pacific Ocean, while the dashed curves refer to stations in the Caribbean. The radial variation

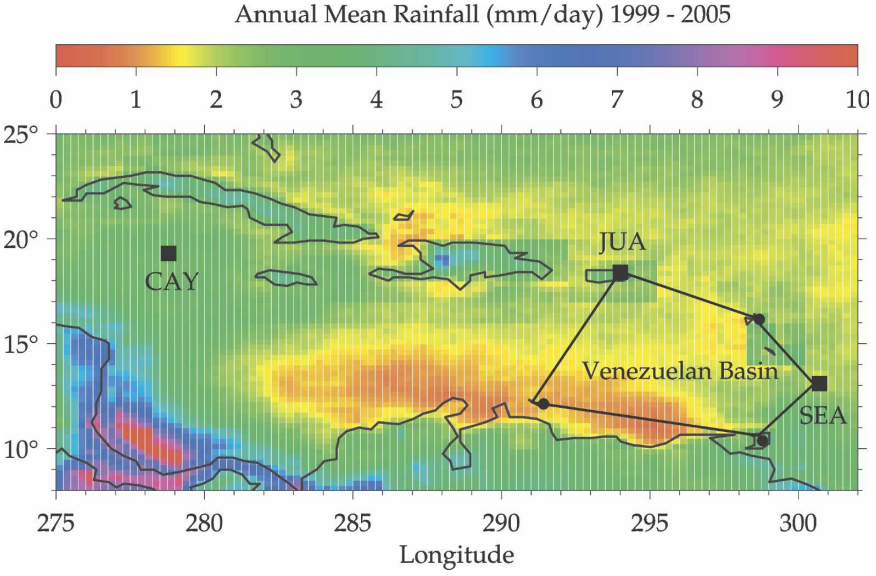


FIG. 3. A map of the Venezuelan Basin array superimposed on TRMM annual mean rainfall. The squares indicate the locations of the U.S. high-resolution radiosonde sites.

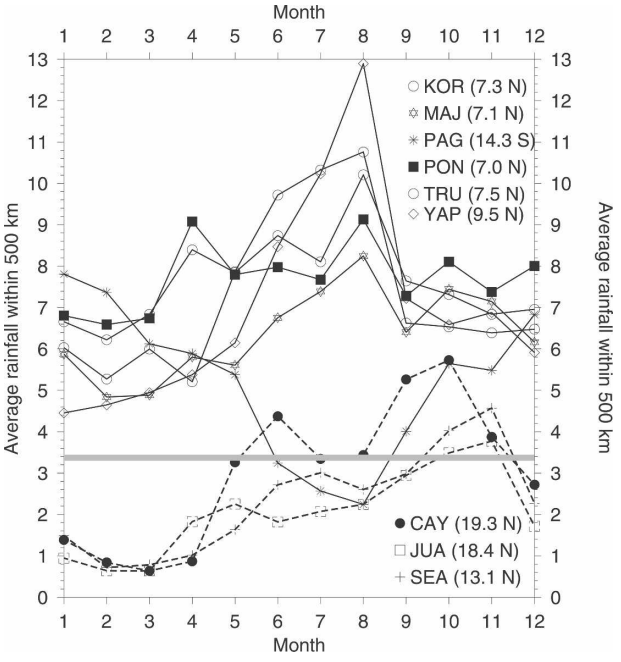


FIG. 4. The monthly mean rainfall rate within a circle with radius of 500 km centered at various islands. Rainfall rates were obtained from the TRMM 3B42 gridded rainfall product. The dashed curves refer to sites in the Caribbean. The horizontal gray line indicates the 3.4 mm day$^{-1}$ rainfall threshold used in the calculation of the temperature anomaly profiles. Each location has been identified by a three-letter code—CAY: Grand Cayman, JUA: San Juan/Isla Verde (U.S.), KOR: Koror/Palau Island, MAJ: Majuro/Marshall Island, PAG: Pago Pago International Airport (Samoa), PON: Ponape Island, SEA: Seawell (Barbados), TRU: Truk International/Moen Island, and YAP: Yap Island.

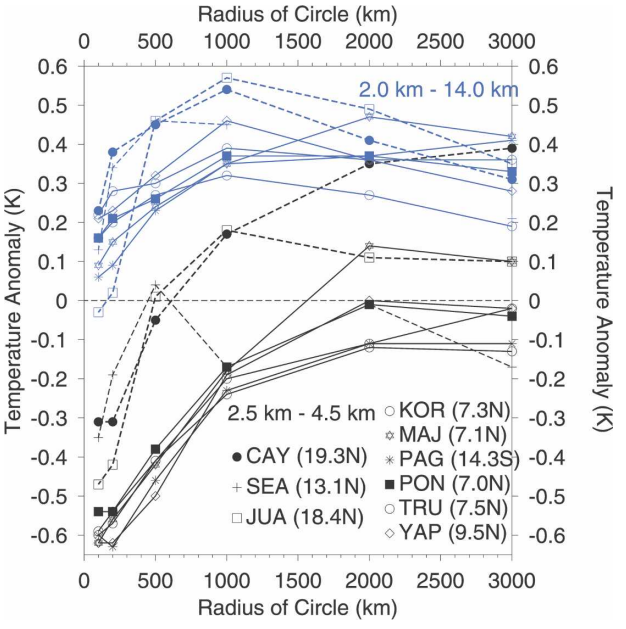


FIG. 5. The convective temperature anomaly (black curves), averaged between 2.5 and 4.5 km, plotted against the radius of the circle within which rainfall is enhanced. Dashed curves refer to radiosonde stations in the Caribbean. The spatial extent of the lower-tropospheric cooling is much larger in the equatorial Pacific than in the Caribbean. The blue curves show the full-depth tropospheric temperature anomaly between 2.0 and 14.0 km. The full-depth warming is slightly larger in the Caribbean than in the equatorial Pacific. The correspondence between the three-letter codes and radiosonde stations is the same as in Fig. 4.

of the full-depth tropospheric warming is quite similar at all stations. However, the lower-tropospheric cold anomalies decay with distance more rapidly at the Caribbean stations than at the Pacific stations. This is generally consistent with the expectation that the Rossby radius of deformation is shorter at higher latitudes. However, despite being located at a latitude that is comparable with that of the Caribbean stations, the lower-tropospheric cooling at Pago Pago (Samoa) decays with distance at a rate that is similar to the more equatorial Pacific stations.

Figure 5 indicates that the lower-tropospheric negative temperature anomalies associated with tropical rainfall decrease with distance approximately exponentially from rainfall source regions, and that the rate of decrease is more rapid in the Caribbean than in the equatorial Pacific. There are, however, a number of confounding factors that complicate the interpretation of this figure. First, the average distance of the rainfall from the radiosonde locations tends to be approximately equal to the radius of the circle divided by $\sqrt{2}$, as would occur if the rainfall were distributed uniformly within each circle. Second, the temporal variability of the average rain rate of the smaller circles is much higher than the temporal variability in the larger circles. At Koror, for example, the 90% and 95% rain-rate percentiles of the 100-km circle occur at 19.5 and 36.5 mm day$^{-1}$ respectively, whereas the corresponding rain rates of the 3000-km circle are 8.3 and 9.3 mm day$^{-1}$. The enhanced rainfall rates used to generate the temperature anomaly profiles shown in Fig. 1 are therefore larger for the smaller circles than for the bigger circles. This effect may partially compensate for the smaller size of the enhanced rainfall regions of the smaller circles. It can also be shown that the average rainfall rate within 100 km of a radiosonde station is positively correlated with the average rainfall rate between 100 and 200 km. The lower-tropospheric temperature anomalies associated with enhanced rainfall within 100 km are therefore partly due to enhanced rainfall at larger distances. Similar considerations apply to the temperature anomaly profiles of other circles. Finally, some of the radiosonde stations are close to large landmasses. Rainfall over land has a stronger diurnal cycle

than rainfall over the ocean and a heating profile that reflects a differing relative mixture of shallow, convective, and stratiform precipitation (Schumacher et al. 2007). The temperature anomaly profile generated by rainfall over land would therefore in general be different from the temperature anomaly profile generated by rainfall over the ocean.

The transition from negative to positive temperature perturbations occurs near the 5-km melting level in each of the temperature anomaly profiles. Radar measurements suggest that ice crystals descending within precipitating stratiform anvil clouds grow rapidly by aggregation as they approach the 0°C level (Houze 1997). This rapid increase in size, and fall speed, would increase the downward flux of condensate near the bottom of the cloud and tend to lock the base of the precipitating stratiform anvil to an altitude near the 5-km melting level. The condensate subsequently melts and evaporates as it falls through unsaturated air beneath the anvil base. This localized cooling helps generate the stratiform gravity waves that communicate this cooling to larger spatial scales (Mapes and Houze 1995). The temperature anomaly patterns shown in Fig. 1 are therefore a compelling illustration of the impact of cloud microphysics on the meso- and large-scale temperature response of the background atmosphere to deep convective heat sources.

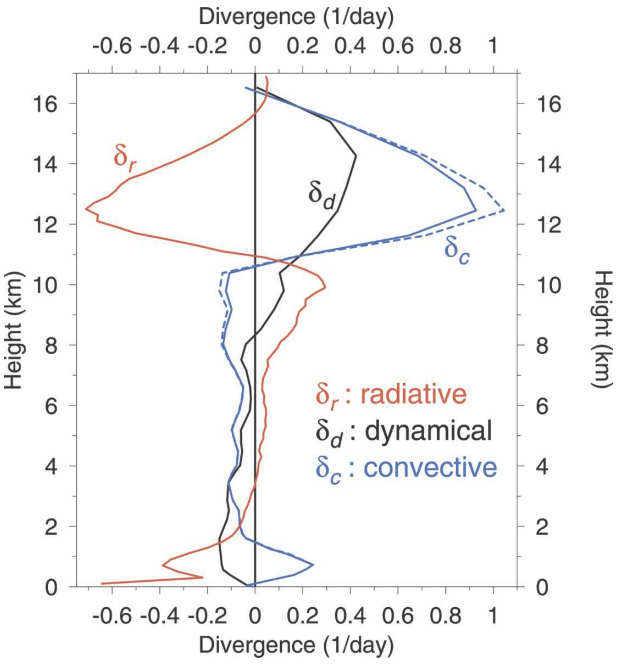


FIG. 6. The dynamical divergence is an average of all divergence profiles from the IFA array during TOGA COARE. The radiative divergence is an annual mean profile calculated from radiosonde temperature and relative humidity profiles from Koror (7.4°N). The convective divergence $\delta_c$ was calculated from the formula $\delta_c = \delta_d - \delta_r$. The dashed blue curve is the convective divergence profile obtained by setting the cloud fraction equal to zero at all heights.

## 3. IFA divergence profiles

The temperature anomaly patterns shown in Fig. 1 are consistent with convectively induced mean downward motion in the background atmosphere above 5 km, and mean upward motion in the background atmosphere below 5 km. One would therefore expect deep convective rainfall to be correlated with a net midlevel convergent inflow from the background atmosphere. Radar and rawinsonde measurements (Mapes and Houze 1995; Mapes et al. 2006), as well as meteorological analyses (Kiladis et al. 2005), confirm that deep convective mesoscale systems are indeed convergent in the midtroposphere.

The black curve in Fig. 6 is the mean dynamical divergence profile $\delta_d$ from the Intensive Flux Array (IFA) of TOGA COARE. This profile is an average of all divergence profiles calculated using horizontal wind measurements from a variety of land- and ship-based rawindsonde measurements from 1 November 1992 to 28 February 1993. The calculated divergence profiles were downloaded from the Colorado State University (CSU) TOGA COARE Sounding Data Archive. The IFA was approximately 200 km in diameter. Its location is shown in Fig. 2. The higher values of dynamical divergence between 10 and 16.5 km reflect deep convective outflow into the background atmosphere. The dynamical divergence is increasingly negative in the lower troposphere, presumably reflecting the midlevel convergence of the stratiform mode, as well as entrainment into deep convective updrafts and downdrafts. It has been shown that if the divergence profile is restricted to periods when deep mesoscale convective systems are present within the IFA, the midlevel convergence is significantly enhanced over that shown in Fig. 6 (Mapes and Houze 1995; Mapes et al. 2006).

The dynamical divergence profile of an array does not directly reflect the net divergence of all convective processes within a domain. One can, however, generate an estimate of the convective divergence by making a correction for the divergence associated with clear sky radiative mass fluxes. Let $\omega_T$ refer to the domain-averaged vertical pressure velocity $\omega_T$ of some region. The dynamical divergence of the region can be expressed as

$$\delta_d = -\frac{\partial \omega_T}{\partial p}. \quad (1)$$

It is useful to conceptually decompose the total vertical mass flux $\omega_T$ of some domain into a component $\omega_r$ associated with the clear sky portion of the domain, and a component $\omega_c$ associated with the cloudy, turbulent, portion of the domain:

$$\omega_T = \omega_r + \omega_c. \tag{2}$$

Both $\omega_r$ and $\omega_c$ are considered to be domain-averaged quantities. Let $f$ refer to the fraction of the domain at each altitude that is occupied by cloud. The domain-averaged clear sky mass flux $\omega_r$ can then be expressed in terms of the clear sky radiative heating $Q_r$ and static stability $\sigma$:

$$\omega_r = (1 - f)\frac{Q_r}{\sigma}. \tag{3}$$

This approximation is valid in the following limits: when the potential temperature surfaces within the domain can be regarded as fixed (a good approximation in the tropics), when the net horizontal transport of heat into or out of a region can be assumed small, and when heating rates in cloud-free regions are not significantly perturbed by the presence of clouds.

We use a cloud fraction profile that peaks at 0.17 near 200 hPa, but is less than 0.05 in most of the rest of the troposphere. These values are consistent with the profiles generated by two 3D cloud-resolving models (Tompkins and Craig 1999; Blossey et al. 2007). They are also roughly consistent with the cloud fractions in various pressure intervals generated by the International Satellite Cloud Climatology Project (ISCCP; Hartmann et al. 2001). The value of the cloud fraction can be expected to display some sensitivity to the width of the pressure interval over which it is defined.

One can relate the convective mass flux to a convective heating rate

$$\omega_c = \frac{Q_c}{\sigma}, \tag{4}$$

where $Q_c$ is the total domain-averaged convective heating rate associated with condensational heating, evaporative cooling, melting and freezing processes, sensible heat flux divergences from turbulence within clouds, and cloud radiative heating. Note that an evaporative downdraft is defined here as occurring within the cloudy, or convective, portion of the domain.

Equations (1) and (2) can be combined as

$$\delta_d = \delta_r + \delta_c. \tag{5}$$

This expression allows the convective divergence $\delta_c$ to be estimated from the dynamical divergence $\delta_d$ (which can be estimated from observations) and the clear sky radiative divergence $\delta_r$ (which can be calculated).

The red line in Fig. 6 is an estimate of the radiative mass flux divergence $\delta_r$ within the IFA. It is an annual mean profile, constructed from monthly mean profiles of temperature and water vapor mixing ratio at Koror, a nearby radiosonde station. Clear sky heating rates were calculated using the Rapid Radiative Transfer Model (RRTM; Mlawer et al. 1997). The heating rates generated by the RRTM agree to within 0.1 K day$^{-1}$ of a line-by-line radiative transfer code. This model currently uses the CKD 2.4 parameterization of the water vapor continuum (Clough et al. 1989).

The blue curve in Fig. 6 is an estimate of the convective divergence within the IFA obtained from (4). Taking the clear sky radiative divergence into account significantly increases the peak amplitude of the deep outflow mode. In general, one would expect the magnitude of the deep outflow mode to scale with the average deep convective rainfall within the domain. The mean rainfall rate within the IFA during the TOGA COARE period was estimated to be 8.42 mm day$^{-1}$ (Ciesielski et al. 2003). This is roughly 2.3 times larger than the tropical mean (20°S–20°N) rainfall rate of 3.6 mm day$^{-1}$, as calculated from the Global Precipitation Climatology Project (GPCP) dataset (Huffman et al. 1997). The maximum upper-level convective divergence within the IFA was approximately 1.0 day$^{-1}$, or 2.5 times larger than the tropical mean (20°S–20°N) upper-level convective divergence of 0.4 day$^{-1}$ (Folkins and Martin 2005).

The dashed blue curve in Fig. 6 is the convective divergence profile generated by setting the cloud fraction equal to zero at all altitudes. Its proximity to the profile generated using the assumed cloud fraction profile shows that the convective divergence is not strongly sensitive to errors in the assumed cloud fraction profile.

Approximately one-half of the upper-level convective divergence within the IFA is balanced internally by radiative convergence. The remainder contributes to the large-scale Hadley–Walker circulation. However, the fraction of the convective outflow, which is balanced by internal radiative descent, is much smaller near the top of the deep outflow layer (e.g., above 14 km). Dynamical divergence profiles therefore tend to overestimate the mean altitude of deep convective outflow. The diminished extent with which convective outflow above 14 km is compensated by induced local radiative descent (or ascent) is due to the weakness of clear sky radiative heating rates at these altitudes.

Figure 6 indicates that deep convective outflow within the IFA extends from roughly 10.5 to 16.5 km. In terms of potential temperature, this corresponds to a range of $\theta$ = 344.5 to $\theta$ = 368 K. The threshold pseudoequivalent potential temperature ($\theta_e$) at which air

parcels in the western tropical Pacific boundary layer first attain positive convective available potential energy (CAPE) is approximately equal to 344.5 K, while 368 K is roughly equal to the maximum $\theta_e$ observed in the boundary layer (Folkins and Braun 2003). The probability distribution of positive CAPE air parcels in the boundary layer therefore appears to have some relationship to the top and bottom altitudes of the deep outflow layer. This is somewhat surprising. The standard definition of pseudoequivalent potential temperature does not account for effects due to the freezing of condensate in increasing the final detrainment potential temperature. Second, modeling studies have demonstrated that deep convective plumes strongly mix with their environment (Kuang and Bretherton 2006). It is possible, however, that the effects of mixing on the final detrainment altitude of air parcels rising from the boundary layer are partially mitigated by the tendency for deep convective plumes to grow in an environment that has been premoistened by shallow convection.

## 4. Dynamical divergence profiles from large-scale arrays

To the extent that deep convection is associated with regional-scale low-level uplift, low-level cooling, and an enhanced occurrence of shallow convection, one would expect the stratiform convergence of deep convective systems to be "screened" by a low-level divergence from surrounding shallow cumuli. Figure 5 suggests that the spatial scale over which this screening would occur is roughly 1000 km in the equatorial Pacific, and 300 km in the Caribbean. This section attempts to determine the effectiveness of this screening mechanism by examining seven dynamical divergence profiles from the western tropical Pacific, and one from the Caribbean Sea.

For the most part, previous estimates of dynamical divergence profiles have been obtained from rawinsonde arrays whose spatial extent was significantly smaller than 1000 km. This approach helps constrain the net vertical mass transport associated with deep convection, but does not provide observational guidance on the nature of the coupling between deep and shallow convection. One motivation for calculating dynamical divergence profiles on larger spatial scales is to determine the extent to which deep and shallow convection are spatiotemporally coupled.

Figure 7 shows the dynamical divergence profiles of eight rawinsonde arrays in the tropics. They were obtained from wind measurements stored at the British Atmospheric Data Center (BADC) archive. The locations of the arrays are shown in Figs. 2 and 3. The dynamical divergence of each array was calculated using the formula

$$\delta_d = (1/A) \oint \mathbf{V}_h \cdot \mathbf{n}\, dl, \tag{6}$$

where $\mathbf{V}_h$ is the horizontal wind vector, $\mathbf{n}$ is a unit vector normal to the lines connecting the stations, $A$ is the area of the array, and $\oint$ is an integral around the boundary of the array.

The $\mathbf{V}_h$ was calculated at the midpoint of each segment of the array by linear interpolation from the two horizontal winds at the endpoints. This introduces an error in the calculation of the divergence profiles, especially when the sites are widely spaced. The climatological dynamical divergence profiles shown in Fig. 7 should, however, be realistic to the extent that (i) the interpolation errors are randomly distributed (i.e., bias errors associated with stationary patterns in the divergent wind are small), and (ii) there are a sufficient number of wind measurements to reduce the random error in the mean divergence profiles to a reasonable value. Horizontal winds from the BADC archive are in principle available from 1996 to 2006. However, the frequency of coverage is not uniform among the sites. Where possible, the dynamical divergence profiles shown in Fig. 7 were calculated from rawinsonde stations with the highest sampling rates. Nevertheless, some of the dynamical divergence profiles are significantly more statistically representative than others. This reflects differences in both the number of rawinsonde stations used to define the ring, as well as the number of complete wind measurements at each pressure level. In terms of the average number of divergence measurements per pressure level used to define the mean rainy profile, the rings have the following ranking from best to worst: Philippines (~2000 per level), equatorial (~700 per level), South China Sea (100–700 per level), the two Bay of Bengal rings (~250 per level), southeast Pacific intertropical convergence zone (SITCZ) (~110 per level), and India and Venezuelan Basin (~50 per level). The statistical representativeness ITCZ and Venezuelan Basin rainy divergence profiles are compromised by the shortness of their rainy seasons.

The two rings surrounding the Bay of Bengal are strongly monsoonal, have three rawinsonde stations in common, and define essentially the same domain. The differences between the dynamical divergence profiles of these two rings demonstrates that the divergence profile does exhibit some sensitivity to the choice of rawinsonde station.

The dynamical divergence profile of an array can be

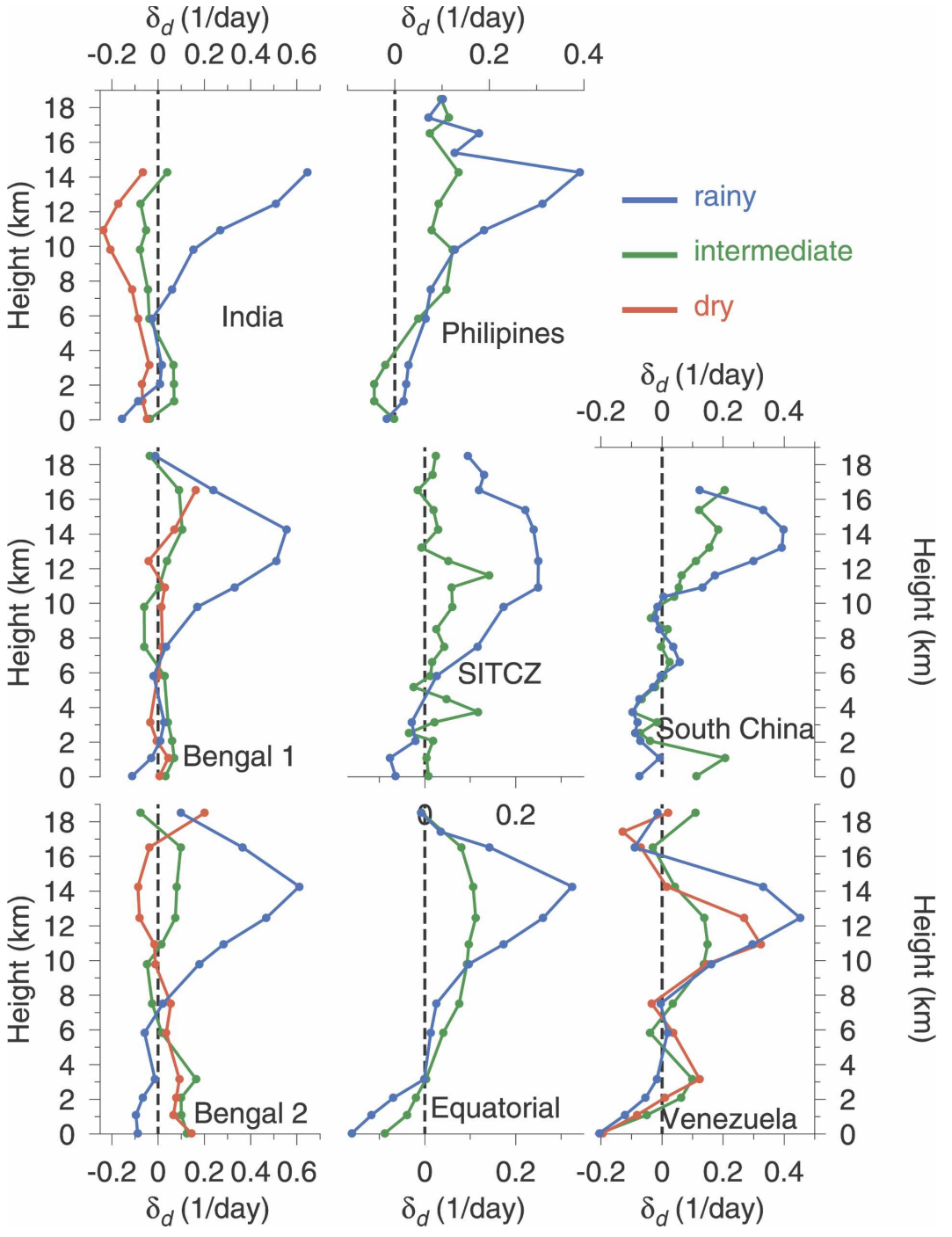


FIG. 7. Dynamical divergence profiles calculated from the rawinsonde arrays shown in Figs. 2 and 3. The rainy profiles shown in blue refer to averages over months in which the mean rainfall exceeded some threshold (usually 6 mm day$^{-1}$). Profiles shown in red refer to averages over months in which the mean rainfall was less than 1.5 mm day$^{-1}$. Profiles shown in green refer to averages in which the monthly mean rainfall rate was larger than 1.5 mm day$^{-1}$ but less than the rainy threshold.

expected to vary seasonally depending on the amount of rainfall inside it. Figure 8 shows the seasonal variation of monthly mean rainfall within each array, obtained using 1999–2005 TRMM 3B42 rainfall rates. Months during which the climatological mean rainfall rate was below 1.5 mm day$^{-1}$ were considered "dry." The average divergence profile from all divergence profiles in this category is shown as red in Fig. 7. Months

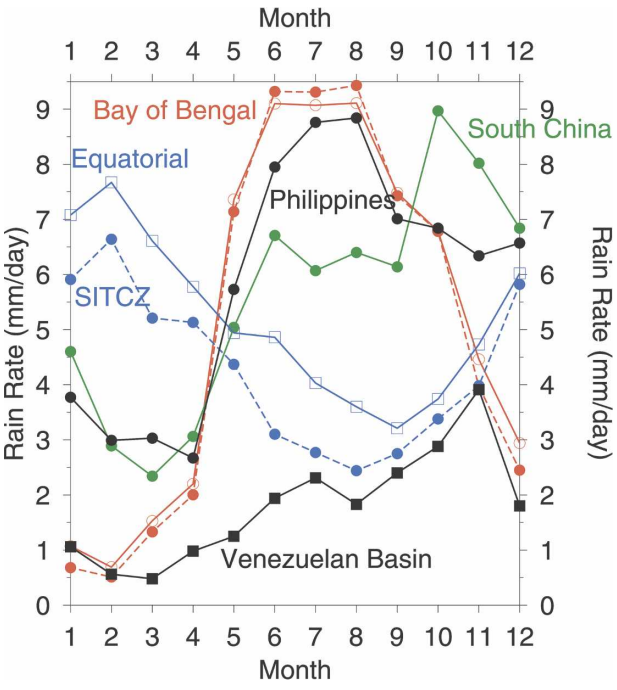


FIG. 8. The seasonal variation of monthly mean rainfall within the arrays shown in Figs. 2 and 3.

during which the average rainfall rate was above some threshold were assumed to be in the "rainy" category. This threshold was set equal to 6 mm day$^{-1}$ for all arrays except the Venezuelan Basin. Because the average rainfall in this array was much less than those in the Pacific, its rainy threshold was set equal to 3 mm day$^{-1}$. The divergence profiles generated by averaging over all rainy months are shown as blue in Fig. 7. Divergence profiles from months with rainfall rates falling between these two rates were assigned to an "intermediate" category and are shown in green. As would be expected, the upper-tropospheric divergence maxima of the blue rainy divergence profiles are much stronger than those of the other two categories.

The left-hand side of Fig. 9 is a compilation of the rainy dynamical divergence profiles from seven of the eight arrays. Each of the profiles exhibits pronounced outflow in the upper troposphere, and near-zero dynamical divergence between 2 and 7 km. The right-hand side of Fig. 9 shows annual mean radiative divergence profiles from five radiosonde locations in the western equatorial Pacific characterized by high rainfall rates. These profiles exhibit weak radiative divergence in the interval between 2 and 7 km. This feature has also been seen in other radiative divergence profiles (Kubar et al. 2007).

If both the dynamical and radiative divergence of a region are near zero in some height interval, Eq. (5) indicates that the convective divergence within that region should also be near zero. The convective divergence refers to the total divergence from both deep and shallow convection. For the dynamical divergence profiles shown in Fig. 9, the convective divergence from shallow convective clouds must therefore cancel, or screen, the midlevel convergence from deep convection. Although this is clearly not a general property of tropical deep convection, Fig. 9 suggests that it does occur in regions in which there is enhanced rainfall (i.e., more than 6 mm day$^{-1}$ in the equatorial Pacific), and where the divergence is averaged over spatial scales on the order of 1000 km or larger.

The climatological divergence profiles shown in Fig. 7 also reflect significant averaging in time. Because of the spatial and temporal gaps in any rawinsonde measurement of domain-averaged divergence, it is not possible to separately determine the spatial and temporal scales over which screening takes place. Presumably, however, these scales must be sufficiently large to average over the complete life cycle of the largest convective systems within the domain.

Model simulations have shown that deep convection stimulates the growth of shallow convection on a spatial scale that is similar to the distance over which deep convection cools and destabilizes the lower troposphere (Tulich et al. 2007). Figure 5 indicates that in the equatorial Pacific, this distance is approximately 1000 km. The dynamical divergence profile of a region with locally enhanced deep convective rainfall, but with a spatial extent smaller than 1000 km, might be expected to be convergent in the lower troposphere because some fraction of the induced shallow convection would be occurring outside the domain. The IFA and South China Sea rings appear to be examples of this type. Both rings have a spatial scale substantially smaller than 1000 km, a rainfall rate that is enhanced relative to their surroundings, and as shown in Figs. 6 and 7, are both convergent in the lower troposphere.

The divergence profiles shown in Fig. 7 were obtained by averaging over all profiles in which the climatological monthly rainfall inside each ring occurred within a particular range. Figure 10 shows the divergence profiles of the equatorial and Philippines rings, obtained by averaging over all divergence profiles based on the instantaneous rainfall rate within each ring. As would be expected, the upper-tropospheric divergence increases as the average rain rate increases. This behavior supports the notion that one can construct physically representative divergence profiles from a limited number of rawinsonde stations, provided one averages over a sufficiently large number of mea-

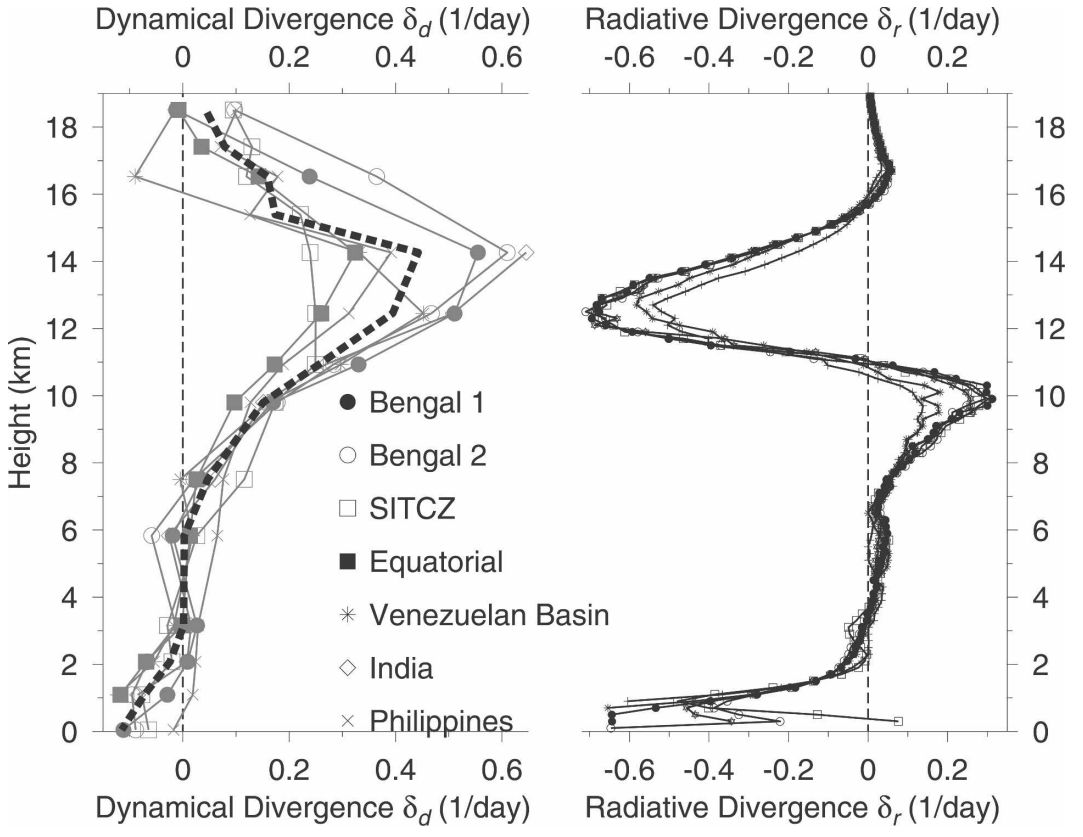


FIG. 9. (left) Seven of the eight rainy divergence profiles shown in Fig. 7 (South China is not shown since it has a size <1000 km). The thick dashed line is an average of all seven rainy divergence profiles. (right) The annual mean radiative mass flux divergence $\delta_r$ profiles at five equatorial Pacific radiosonde stations: Koror, Truk, Majuro, Yap, and Ponape.

surements. In these profiles, the magnitude of the divergence between 3 and 8 km tends to decrease as the upper-level divergence increases. This decrease would not occur in the absence of some degree of cancellation between the midlevel convergence from deep convection and the divergent outflow from shallow convection.

The local surface pressure tendency can be expressed as a vertical pressure integral of the dynamical divergence from the surface to the top of the atmosphere. Within each array, average surface pressure would be expected to evolve slowly over time. One would therefore expect the vertically integrated dynamical divergence to be near zero: outflow in the upper atmosphere should be mostly compensated by inflow near the surface. However, it can be shown that most of the dynamical divergence profiles shown in Fig. 7 tend to export more mass in the upper troposphere than they import in the boundary layer. The magnitude of this imbalance is exacerbated by the use of height rather than pressure as a vertical coordinate. The imbalance may reflect the difficulty of estimating the magnitude of the convergence in the boundary layer, where turbulence and sea breeze circulations would play a relatively greater role in undermining a relationship between the local- and large-scale wind fields.

The weakness of the dynamical divergence in the mid- and lower troposphere, when spatially and temporally averaged over sufficiently large actively convecting regions, suggests that deep convection is associated with a closed regional low-level circulation in which midlevel inflow is balanced by outflow from shallow convection. Figure 11 shows a cartoon of this low-level circulation, together with the upper-level Hadley–Walker circulation. The existence of two distinct tropical circulations has been previously inferred from an examination of National Centers for Environmental Prediction (NCEP) and European Centre for Medium-Range Weather Forecasts (ECMWF) analyses (Trenberth et al. 2000). The global monsoon mode was associated with deep divergent outflow peaking at 150 hPa (~14 km), while the second monsoon mode with shallow divergent outflow peaked between 750 and 350 hPa.

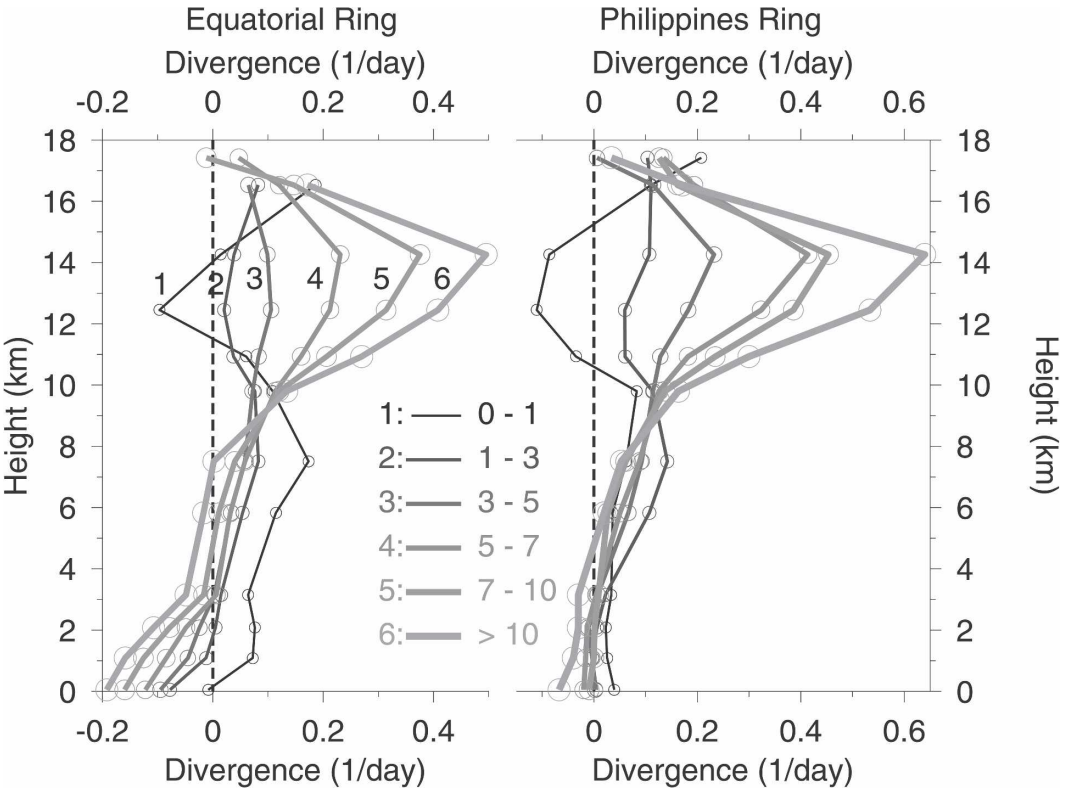


FIG. 10. (left) The response of the mean dynamical divergence of the equatorial ring to increased precipitation. The curves labeled 1–6 correspond to averages over individual divergence profiles when the instantaneous rain rate within the ring was 0–1, 1–3, 3–5, 5–7, 7–10, and >10 mm day$^{-1}$. (right) The response of dynamical divergence profiles of the Philippines ring to increased precipitation.

## 5. Lapse rates in the lower troposphere

In actively convecting regions, the mean temperature profile of the background atmosphere can be considered a collective response to the spectrum of irreversible vertical motions imposed on the background atmosphere by all convectively generated gravity waves. Figure 1 suggests that downdrafts play a relatively greater role in determining the mesoscale temperature response to deep convection below the 5-km melting level than in the rest of the troposphere. One might therefore expect the 5-km melting level to be also associated, in some way, with a change in the mean temperature profile. Figure 12 shows the vertical variation of the seasonal mean lapse rate at Koror. The melting level is indeed associated with a local maximum in stability, as is the top of the boundary layer (~2 km).

The lapse rate in Fig. 12 was calculated using virtual temperature rather than temperature. At a given pressure, the virtual temperature of an air parcel has a direct relationship with density. Because gravity waves are generated by density anomalies, it is probably more appropriate to think of convection as driving the atmosphere toward a particular density profile than a particular temperature profile. Observations have demonstrated that vertical velocities and buoyancy accelerations within tropical updrafts and downdrafts are small (Jorgensen and LeMone 1989). This would suggest that, in the tropics, the time scale with which convective buoyancy anomalies (i.e., updrafts and downdrafts)

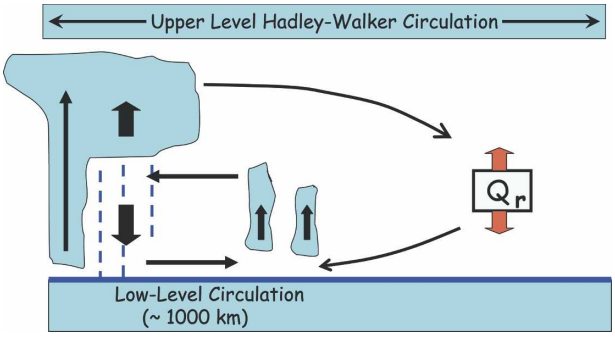


FIG. 11. A schematic plot of the thermodynamic forcings associated with the upper-level Hadley–Walker circulation and the shallow downdraft circulation.

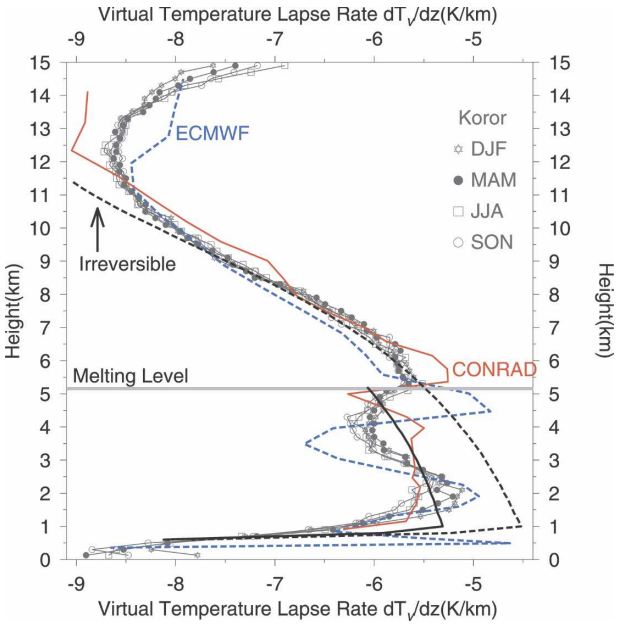


FIG. 12. Seasonal mean profiles of the virtual temperature lapse rate (gray curves) obtained using high–vertical resolution radiosonde profiles at Koror (7.4°N). The dashed black line shows the lapse rate of a moist pseudoadiabat having $\theta_{ep}$ = 352 K and a relative humidity at the surface of 75%. The solid black line shows the density temperature lapse rate of a reversible moist adiabat, also with $\theta_e$ = 352 K, and a relative humidity at the surface of 75%. The dashed blue line shows a virtual temperature lapse rate from the July 2004 ECMWF analysis, averaged from 0°–10°N and 140°–180°E. The solid red curve is the virtual temperature lapse rate from the one-dimensional CONRAD model.

mutually equilibrate to a common density profile with the background atmosphere is fairly short.

One often thinks of the tropical temperature profile as approximating a moist adiabat. Figure 12 shows the lapse rates generated by reversible and irreversible moist adiabats, each having an equivalent potential temperature of 352 K and a relative humidity at the surface equal to 75%. A reversible adiabat is one in which the rising air parcel is assumed to retain all condensate. Above the 0°C melting level, the density temperature lapse rate of the reversible adiabat becomes sensitive to the assumed phase of the retained condensate, and is not shown. An irreversible moist adiabat is one in which all condensate is assumed to be immediately removed. In this case, the density temperature reduces to the virtual temperature.

Above the melting level, the observed virtual temperature lapse rate at Koror is virtually coincident with the lapse rate of the 352-K irreversible moist pseudoadiabat. Below the melting level, the magnitude of the observed lapse rate is in better agreement with the reversible adiabat. However, neither the reversible or irreversible adiabats are able to reproduce the shape of the observed lapse rate profile between 2 and 5 km. This is also the interval where some models appear to have difficulty simulating the observed density profile. The dashed blue line in Fig. 12 is a virtual temperature lapse rate obtained from an atmospheric model analysis produced by ECMWF. This model has 0.5° horizontal resolution and 60 levels from the surface to 60 km. There are 35 levels in the troposphere. The lapse rate profile shown in Fig. 12 is a July 2004 average between 0°–10°N and 140°–180°E. It exhibits a very pronounced lower-tropospheric dipole not seen in the observations.

The red line in Fig. 12 is the virtual temperature lapse rate generated by a one-dimensional model based on a convective parameterization (Emanuel and Živković-Rothman 1999). The version used here is coupled to an interactive radiative transfer model with more complete cloud physics that uses a fractional cloud scheme (Bony and Emanuel 2001), and will be referred to as the CONRAD (Emanuel) model. It is run with a fixed sea surface temperature of 27.5°C and vertical resolution of 25 hPa. Although it simulates the density of the lower troposphere more realistically than the ECMWF analysis, it does not reproduce the "notch," or indentation, in the observed profile between 2 and 5 km.

It may be impossible to accurately reproduce the observed lower-tropospheric lapse profile in specific tropical regions in the context of a one-dimensional model. The observed lapse rate may reflect the large-scale heating structure of the tropics, or the regional low-level circulation of actively convecting regions. When dynamically forced by an observed divergence field, the CONRAD model was able to more realistically simulate the lower-tropospheric lapse rate observed within the IFA during TOGA COARE (Bony and Emanuel 2001).

Figure 13 shows annual mean vertical profiles of static stability $\sigma$ at the five high–vertical resolution U.S. radiosonde stations in the western Pacific. The static stability is closely related to the lapse rate, and also exhibits a notch between 2 and 5 km. The blue curves in Fig. 13 show the vertical variation of annual mean clear sky heating rates at the five locations. The red curves show the clear sky radiative mass flux $\omega_r$ obtained from the corresponding heating rate and static stability. Between 2 and 7 km, the static stability and heating rate tend to vary with altitude in a similar manner. This covariation suppresses the vertical variation of the clear sky mass flux and contributes to the weakness, as shown in Fig. 9, of the clear sky radiative divergence $\delta_r$ between 2 and 7 km.

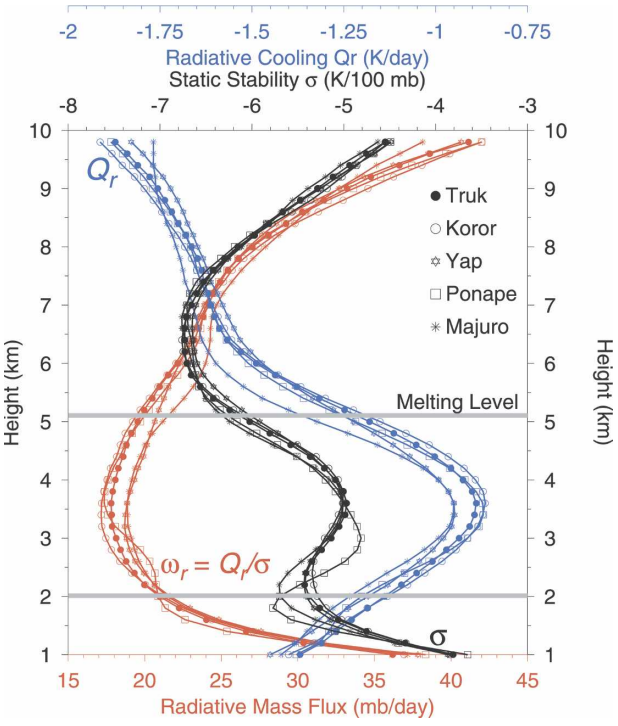


FIG. 13. Annual mean profiles of static stability $\sigma$ (black curves) at the five high-resolution U.S. radiosonde stations in the western Pacific: Koror, Truk, Majuro, Yap, and Ponape. The blue curves represent annual mean radiative heating profiles $Q_r$. The clear sky radiative mass flux profiles were calculated using $\omega_r = Q_r/\sigma$, and are shown in red.

## 6. Summary

The main purpose of this paper is to provide additional evidence, and some thermodynamic context, for the existence of a closed regional low-level circulation in actively convecting regions of the tropics. The argument that this circulation is closed requires that the lower-tropospheric dynamical divergence does indeed go to zero in actively convecting regions, when averaged over sufficiently large spatiotemporal scales. There are errors associated with calculating dynamical divergence profiles over large regions using a relatively sparse rawinsonde network. We have tried to reduce these errors by averaging over many years of data, and by examining the profiles of several different regions. The argument that the divergent component of this circulation arises primarily from precipitating shallow convection, while the convergent component arises primarily from evaporative cooling within stratiform downdrafts, requires that the clear sky radiative mass fluxes shown here be realistic. The two dominant sources of error in this calculation are probably the perturbations in radiative heating rates of clear sky regions due to nearby clouds, and the possible impact of further refinements in the parameterization of the water vapor continuum on lower-tropospheric heating rates.

Shallow convective rainfall occurs over broad regions of the tropical oceans where deep convection is very infrequent (Schumacher and Houze 2003). Our conclusions on the nature of the coupling between deep and shallow convection are statistical in character and refer only to (i) the high rainfall regime where this coupling would be expected to be strongest, and (ii) regions in which the spatial scale of this high rainfall region is larger than the spatial scale over which lower-tropospheric heat sources are likely to interact (~1000 km). It would be desirable to have more direct observational evidence on the extent to which enhanced deep convection is associated with more frequent shallow convection. However, many field programs have demonstrated that deep and shallow convection are spatiotemporally coupled on both small and large scales (Kiladis et al. 2005; Mapes et al. 2006). The inability of the tropical atmosphere to sustain a net dynamical or radiative mass flux divergence in the mid- and lower troposphere may provide some guidance on the dynamical origin of this coupling.

We have also shown that the lower-tropospheric cold anomalies associated with deep convection have a spatial range of roughly 1000 km in the equatorial Pacific and roughly 300 km in the Caribbean. The full-depth warming associated with deep convection has a much longer spatial range. The tendency for deep and shallow convection to be spatiotemporally coupled may play a role in the more rapid damping of the lower-tropospheric cooling. For example, the shallow convective heating may project onto the cold phase of some of the stratiform gravity waves, thus dissipating them more efficiently.

In actively convecting regions, the lapse rate varies with altitude between 2 and 5 km in a manner that is inconsistent with a moist adiabat. This anomalous variation in lapse rate was not accurately simulated by a high-resolution model analysis. It may, however, be possible to interpret this observed variation in lapse rate as a consequence of the tendency of the dynamical and convective divergence to tend to zero, when averaged over spatial scales of ~1000 km.

*Acknowledgments.* We are grateful for comments on the manuscript by Courtney Schumacher, Robert Fovell, and two anonymous reviewers. The rainfall data used in this study were acquired as part of the Tropical Rainfall Measuring Mission. The algorithms were de-

veloped by the TRMM Science Team. The data were processed by the TRMM Science Data and Information System (TSDIS) and the TRMM Office; they are archived and distributed by the Goddard Distributed Active Archive Center. TRMM is an international project jointly sponsored by the Japan National Space Development Agency (NASDA) and the U.S. National Aeronautics and Space Administration (NASA) Office of Earth Sciences. The IFA average divergence profile was obtained from 3-hourly divergence profiles archived at tornado.atmos.colostate.edu/togadata/ifa_data.html. We thank the Natural Sciences and Engineering Research Council of Canada, the Modeling of Global Chemistry for Climate (GCC) project, and the Canadian Foundation for Climate and Atmospheric Sciences (CFCAS) for their support. The NOAA/NCDC high-resolution radiosonde data were provided by the SPARC data center from their Web site (http://www.sparc.sunysb.edu/html/hres.html). We thank the British Atmospheric Data Center for access to the rawinsonde winds.

## REFERENCES

Betts, A. K., 1973: A composite mesoscale cumulonimbus budget. *J. Atmos. Sci.,* **30,** 597–610.

Blossey, P. N., C. S. Bretherton, J. Cetrone, and M. Khairoutdinov, 2007: Cloud-resolving model simulations of KWAJEX: Model sensitivities and comparisons with satellite and radar observations. *J. Atmos. Sci.,* **64,** 1488–1508.

Bony, S., and K. A. Emanuel, 2001: A parameterization of the cloudiness associated with cumulus convection: Evaluation using TOGA COARE data. *J. Atmos. Sci.,* **58,** 3158–3183.

Ciesielski, P. E., R. H. Johnson, P. T. Haertel, and J. Wang, 2003: Corrected TOGA COARE sounding humidity data: Impact on diagnosed properties of convection and climate over the warm pool. *J. Climate,* **16,** 2370–2384.

Clough, S. A., F. X. Kneizys, and R. W. Davies, 1989: Line shape and the water vapor continuum. *Atmos. Res.,* **23,** 229–241.

Dessler, A. E., S. P. Palm, and J. D. Spinhirne, 2006: Tropical cloud-top height distributions revealed by the Ice, Cloud, and Land Elevation Satellite (ICESat)/Geoscience Laser Altimeter System (GLAS). *J. Geophys. Res.,* **111,** D12215, doi:10.1029/2005JD006705.

Emanuel, K. A., and M. Živković-Rothman, 1999: Development and evaluation of a convection scheme for use in climate models. *J. Atmos. Sci.,* **56,** 1766–1782.

Folkins, I., 2006: Convective damping of buoyancy anomalies and its effect on lapse rates in the tropical lower troposphere. *Atmos. Chem. Phys.,* **6,** 1–12.

——, and C. Braun, 2003: Tropical rainfall and boundary layer entropy. *J. Climate,* **16,** 1807–1820.

——, and R. V. Martin, 2005: The vertical structure of tropical convection and its impact on the budgets of water vapor and ozone. *J. Atmos. Sci.,* **62,** 1560–1573.

Fovell, R. G., G. L. Mullendore, and S.-H. Kim, 2006: Discrete propagation in numerically simulated nocturnal squall lines. *Mon. Wea. Rev.,* **134,** 3735–3752.

Grabowski, W. W., 2003: MJO-like coherent structures: Sensitivity simulations using the cloud-resolving convection parameterization (CRCP). *J. Atmos. Sci.,* **60,** 847–864.

Hartmann, D. L., L. A. Moy, and Q. Fu, 2001: Tropical convection and the energy balance at the top of the atmosphere. *J. Climate,* **14,** 4495–4511.

Houze, R. A., Jr., 1989: Observed structure of mesoscale convective systems and implications for large-scale heating. *Quart. J. Roy. Meteor. Soc.,* **115,** 425–461.

——, 1997: Stratiform precipitation in regions of convection: A meteorological paradox? *Bull. Amer. Meteor. Soc.,* **78,** 2179–2196.

Huffman, G. J., and Coauthors, 1997: The Global Precipitation Climatology Project (GPCP) combined precipitation dataset. *Bull. Amer. Meteor. Soc.,* **78,** 5–20.

Jensen, M. P., and A. D. Del Genio, 2006: Factors limiting convective cloud-top height at the ARM Nauru Island climate research facility. *J. Climate,* **19,** 2105–2117.

Johnson, R. H., T. M. Rickenbach, S. A. Rutledge, P. E. Ciesielski, and W. H. Schubert, 1999: Trimodal characteristics of tropical convection. *J. Climate,* **12,** 2397–2418.

Jorgensen, D. P., and M. A. LeMone, 1989: Vertical velocity characteristics of oceanic convection. *J. Atmos. Sci.,* **46,** 621–640.

Kiladis, G. N., K. H. Straub, and P. T. Haertel, 2005: Zonal and vertical structure of the Madden–Julian oscillation. *J. Atmos. Sci.,* **62,** 2790–2809.

Kuang, Z., and C. S. Bretherton, 2006: A mass-flux scheme view of a high-resolution simulation of a transition from shallow to deep cumulus convection. *J. Atmos. Sci.,* **63,** 1895–1909.

Kubar, T. L., D. L. Hartmann, and R. Wood, 2007: Radiative and convective driving of tropical high clouds. *J. Climate,* **20,** 5510–5526.

Mapes, B. E., 2001: Water's two scale heights: The moist adiabat and the radiative troposphere. *Quart. J. Roy. Meteor. Soc.,* **127,** 2353–2366.

——, and R. A. Houze Jr., 1995: Diabatic divergence profiles in western Pacific mesoscale convective systems. *J. Atmos. Sci.,* **52,** 1807–1828.

——, S. Tulich, J. Lin, and P. Zuidema, 2006: The mesoscale convection life cycle: Building block or prototype for large-scale tropical waves? *Dyn. Atmos. Oceans,* **42,** 3–29.

May, P. T., and D. K. Rajopadhaya, 1996: Wind profiler observations of vertical motion and precipitation microphysics of a tropical squall line. *Mon. Wea. Rev.,* **124,** 621–633.

Mlawer, E. J., S. J. Taubman, P. D. Brown, M. J. Iacono, and S. A. Clough, 1997: RRTM, a validated correlated-*k* model for the longwave. *J. Geophys. Res.,* **102,** 16 663–16 682.

Redelsperger, J.-L., D. B. Parsons, and F. Guichard, 2002: Recovery processes and factors limiting cloud-top height following the arrival of a dry intrusion observed during TOGA COARE. *J. Atmos. Sci.,* **59,** 2438–2457.

Schumacher, C., and R. A. Houze Jr., 2003: The TRMM precipitation radar's view of shallow, isolated rain. *J. Appl. Meteor.,* **42,** 1519–1524.

——, M. H. Zhang, and P. E. Ciesielski, 2007: Heating structures of the TRMM field campaigns. *J. Atmos. Sci.,* **64,** 2593–2610.

Sherwood, S. C., 1999: Convective precursors and predictability in the tropical western Pacific. *Mon. Wea. Rev.,* **127,** 2977–2991.

——, T. Horinouchi, and H. A. Zeleznik, 2003: Convective impact on temperatures observed near the tropical tropopause. *J. Atmos. Sci.,* **60,** 1847–1856.

Tompkins, A. M., 2001: Organization of tropical convection in low vertical wind shears: The role of water vapor. *J. Atmos. Sci.,* **58,** 529–545.

——, and G. C. Craig, 1999: Sensitivity of tropical convection to sea surface temperature in the absence of large-scale flow. *J. Climate,* **12,** 462–476.

Trenberth, K. E., D. P. Stepaniuk, and J. M. Caron, 2000: The global monsoon as seen through the divergent atmospheric circulation. *J. Climate,* **13,** 3969–3993.

Tulich, S. N., D. A. Randall, and B. E. Mapes, 2007: Vertical-mode and cloud decomposition of large-scale convectively coupled gravity waves in a two-dimensional cloud-resolving model. *J. Atmos. Sci.,* **64,** 1210–1229.

Yanai, M., S. Esbensen, and J. Chu, 1973: Determination of bulk properties of tropical cloud clusters from large-scale heat and moisture budgets. *J. Atmos. Sci.,* **30,** 611–627.

Zipser, E. J., 1977: Mesoscale and convective-scale downdrafts as distinct components of squall-line structure. *Mon. Wea. Rev.,* **105,** 1568–1589.